nature physics

Article

https://doi.org/10.1038/s41567-025-03032-2

Observation of the Yamaji effect in a cuprate superconductor

Received: 4 December 2024

Accepted: 13 August 2025

Published online: 16 September 2025

Check for updates

Mun K. Chan[1] ✉, Katherine A. Schreiber[1], Oscar E. Ayala-Valenzuela[1], Eric D. Bauer[2], Arkady Shekhter[1] & Neil Harrison[1]

The pseudogap state of high-temperature superconducting cuprates, known for its partial gapping of the Fermi surface above the superconducting transition temperature, is believed to hold the key to understanding the origin of Planckian relaxation and quantum criticality. However, the nature of the Fermi surface in the pseudogap state has remained a fundamental open question. Here we report the observation of the Yamaji effect, which appears as a peak in the *c*-axis resistivity at a specific angle of the applied magnetic field, in angle-dependent magnetoresistivity measurements above the critical temperature in the cuprate $HgBa_2CuO_{4+\delta}$. The observation of the Yamaji peak is evidence for small Fermi-surface pockets in the normal state of the pseudogap phase. The small size of the pockets, each estimated to occupy only 1.3% of the Brillouin zone area, is not expected given the absence of long-range broken translational symmetry.

Although evidence for symmetry breaking has been found in the pseudogap phase[1–6], its connection to quantum criticality has not yet been established. For such symmetry breaking to be relevant for quantum criticality, it must also have a direct effect on the Fermi surface[7,8]. Indeed, Fermi-surface reconstruction has been explored extensively in the cuprates through magnetic quantum oscillations and angle-dependent magnetoresistivity measurements[7–9]. Such measurements have revealed a magnetic-field-induced charge-density wave phase[10] that exists at temperatures well below the superconducting transition temperature, T_c (refs. 11,12), and an antiferromagnetic phase present at very low hole dopings[13]. Because these phases are restricted to narrow low-temperature or low-doping regimes, they are not indicative of the broader underdoped region and high temperatures spanned by the pseudogap, depicted in Fig. 1a.

In the pseudogap state at temperatures above T_c, the conspicuous observation of anomalous Fermi arcs in photoemission experiments that do not seem to form closed pockets[14,15] has inspired suggestions of an unconventional Fermi surface[16–18] or even the total absence thereof[15,19,20]. Recent work on $La_{2-y-x}Nd_ySr_xCuO_4$ (Nd-LSCO) (ref. 21) found a change in the angle-dependent magnetoresistivity across the putative pseudogap critical doping, which was reported to be consistent with a transformation from large to small Fermi surfaces. However, it has also been argued[22] that this change could be consistent with a Lifshitz transition resulting from crossing of a van Hove singularity, which does not drastically change the size of the Fermi surface. Therefore, there is a crucial need to clarify the Fermi surface of the pseudogap state.

One way to do this in quasi-two-dimensional (layered) metals, such as the cuprates, is through observation of the Yamaji effect, which describes the phenomena when all quasiparticle orbits on the Fermi surface become degenerate at particular orientations of the magnetic field. The signature of the Yamaji effect in angle-dependent magnetoresistivity is a peak in the interlayer, or *c*-axis, resistivity, ρ_c, when the orientation of the magnetic field is tilted away from the *c* axis[23–25]. One of the criteria for the observation of a Yamaji peak, similar to magnetic quantum oscillations, is that the product of the cyclotron frequency, ω_c, and the transport relaxation time, τ, must be at least of the order of unity, $\omega_c\tau \gtrsim 1$: that is, a non-negligible fraction of electrons must complete a cyclotron orbit without scattering. The cyclotron frequency is given by $\omega_c = eB/m^*$, where B is the magnetic field, m^* is the quasiparticle effective cyclotron mass and e is the electric charge. Therefore, similar to quantum oscillations, the observation of the Yamaji effect is evidence for a Fermi-surface pocket[23–25]. Unlike quantum oscillations, which can be observed only at low temperatures when cyclotron orbits are quantized[26], the Yamaji effect does not require orbital quantization. In this respect, the Yamaji effect is much better suited for Fermi-surface

[1]Pulsed Field Facility, National High Magnetic Field Laboratory, Los Alamos National Laboratory, Los Alamos, NM, USA. [2]Los Alamos National Laboratory, Los Alamos, NM, USA. ✉e-mail: mkchan@lanl.gov

https://doi.org/10.1038/s41567-025-03032-2

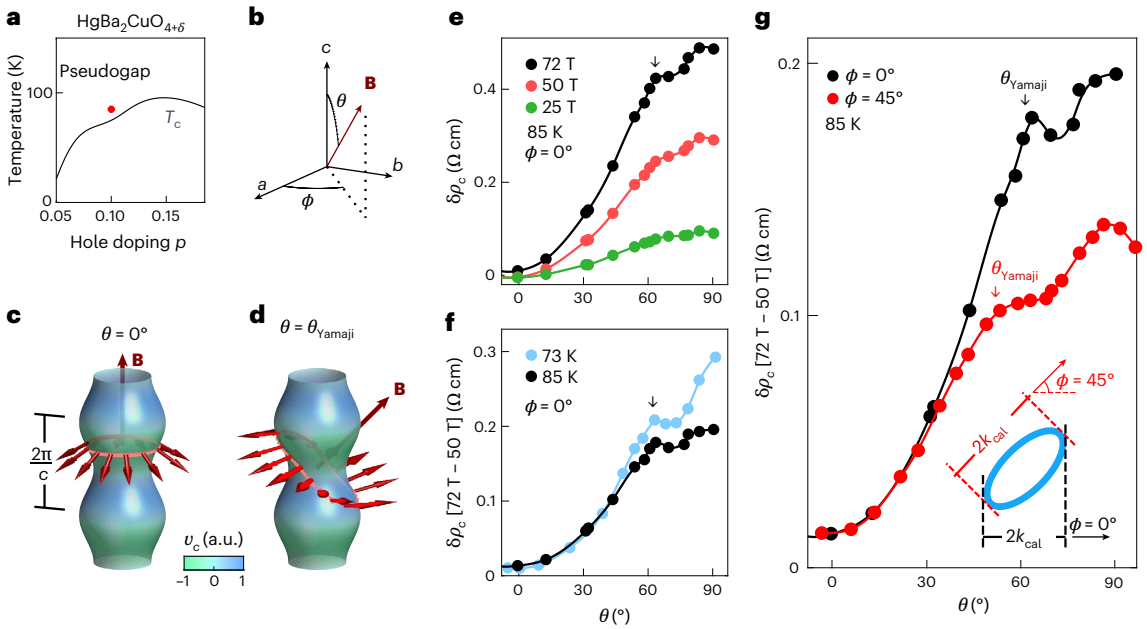

Fig. 1 | Observation of the Yamaji effect. a, Phase diagram of superconducting temperature versus doping of Hg1201 (ref. 47). The red dot marks the focus of this work. **b**, Schematic of the polar (θ) and azimuthal (ϕ) angles. *a*, *b* and *c* are crystallographic directions. **c**, Schematic example orbit on a quasi-two-dimensional Fermi surface with simple sinusoidal warping for $B\|c$. Red arrows indicate the instantaneous velocity on the orbit. The *c*-axis component of the velocity, v_c, does not change on the orbit. **d**, Schematic of example orbit for $\theta = \theta_{\text{Yamaji}}$. The value of v_c oscillates around the orbit and averages to zero. **e**, Polar magnetic field orientation-dependent curves of the *c*-axis magnetoresistivity $\delta\rho_c = \rho_c(B) - \rho_c(0)$ at three different fields, and at 85 K and $\phi = 0°$. The zero field resistivity is $\rho_c(0) = 1.61\ \Omega$ cm. The arrow highlights the Yamaji peak, which disappears into the background at lower *B* due to the lower $\omega_c\tau$. **f**, The Yamaji peak for two different temperatures. The peak is more pronounced at lower temperature due to a higher $\omega_c\tau$. **g**, Azimuthal-angle dependence of the Yamaji peak at $\phi = 0°$ and 45°. The inset schematically shows the relationship between caliper radius $k_{\text{cal}}(\phi)$ and ϕ for an elliptical pocket. In **f** and **g**, we have plotted $\delta\rho_c[72\text{ T} - 50\text{ T}] \equiv \rho_c(72\text{ T}) - \rho_c(50\text{ T})$ to isolate the high field phenomena and to reduce the effect of superconductivity for the lower-temperature data. This permits a more accurate determination of θ_{Yamaji}. Solid lines in **f**–**g** are guides to the eye.

studies at the temperatures above T_c and can be used to study the pseudogap phase from which the high-T_c superconductivity emerges.

Observation of the Yamaji effect

Here we concern ourselves primarily with the magnetic-field-induced change in *c*-axis resistivity $\delta\rho_c = \rho_c(B) - \rho_c(0)$, or magnetoresistivity. Figure 1 shows angle-dependent magnetoresistivity of an underdoped cuprate $HgBa_2CuO_{4+\delta}$ (Hg1201) with a hole doping $p = 0.10$, measured above its superconducting temperature of $T_c = 74$ K. In a static magnetic field, one can rotate the polar angle, θ, while recording ρ_c in situ[21,27]. However, achieving high values of $\omega_c\tau$ at elevated temperatures in the cuprates requires the use of pulsed magnetic fields. Each point of the angle-dependent $\delta\rho_c$, such as those shown in Fig. 1e, is obtained from an individual high-magnetic-field sweep (see Methods for measurement details and Extended Data Figs. 1–3 for all field sweeps and details of pulsed-field magnetoresisitvity measurements).

The Yamaji effect is evident as a local maximum (that is, away from $\theta = 90°$) in $\delta\rho_c$ plotted against θ, indicated by the arrow in Fig. 1e. Figure 1e,f shows that the angular position of the peak, down arrows, does not shift with temperature or magnetic field. It does, however, shift with the azimuthal angle of the magnetic field, ϕ (Fig. 1g)[24,25]. The peak also becomes weaker and eventually fades into the background with decreasing *B*, as shown in Fig. 1e. As we describe below, the Yamaji peak is a consequence of a quasi-two-dimensional Fermi pocket with simple interlayer warping[23].

The Yamaji effect results fundamentally from the *c*-axis hopping of electrons between layers, which causes warping (or corrugation) of what would otherwise be a cylindrical Fermi surface, as shown schematically in Fig. 1c,d (refs. 24,25). The simple tetragonal structure of Hg1201 (ref. 28) leads to warping captured by the lowest-harmonic sinusoidal (see the dispersion relationship given in equation (3) of Methods).

The effect of such simple warping on the conductivity is understood by examining the velocity evolution along classical trajectories on the Fermi surface under the action of the Lorentz force. For the *c*-axis conductivity, σ_c, it suffices to trace only the *c*-axis projection of the velocity on the Fermi surface, v_c, along the quasiparticle trajectory. Specifically, σ_c is proportional to the Fourier transform of the time-delayed velocity correlation,

$$\sigma_c(\omega) \propto \langle v_c(\omega)v_c(-\omega)\rangle = \int_0^\infty \mathrm{d}t \exp\{\mathrm{i}\omega t\}\langle v_c(t)v_c(0)\rangle_{\mathbf{k}}.$$

The time-delayed velocity correlation $\langle v_c(t)v_c(0)\rangle_{\mathbf{k}}$, is averaged over all possible starting points **k** on the Fermi surface[24,25]. The resistivity ρ_c is then obtained by inverting the conductivity $\sigma_c(\omega)$ and taking the zero-frequency limit.

Factors that contribute to a large *c*-axis magnetoresistivity include how effectively the v_c around a cyclotron orbit averages to zero, and how far a quasiparticle can travel around the orbit before scattering. In the clean limit, when $\omega_c\tau \gg 1$, electrons can traverse the cyclotron orbit multiple times and the conductivity corresponds to the velocity averaged over a single complete orbit. As the scattering becomes more intense, and $\omega_c\tau$ decreases, the time-delayed velocity correlation is suppressed at long times. The magnetic field dependence of the *c*-axis resistivity weakens and eventually disappears in the dirty limit, $\omega_c\tau \ll 1$. Such a physical picture enables a qualitative understanding of the results in Fig. 1.

When *B* is aligned along the *c* axis, v_c does not change around any given orbit for the simply warped Fermi surface ($\theta = 0°$ in Fig. 1c). Hence, the conductivity at finite *B* is the same as that at $B = 0$. On rotating the magnetic field away from the *c* axis, the cyclotron orbital trajectories

https://doi.org/10.1038/s41567-025-03032-2

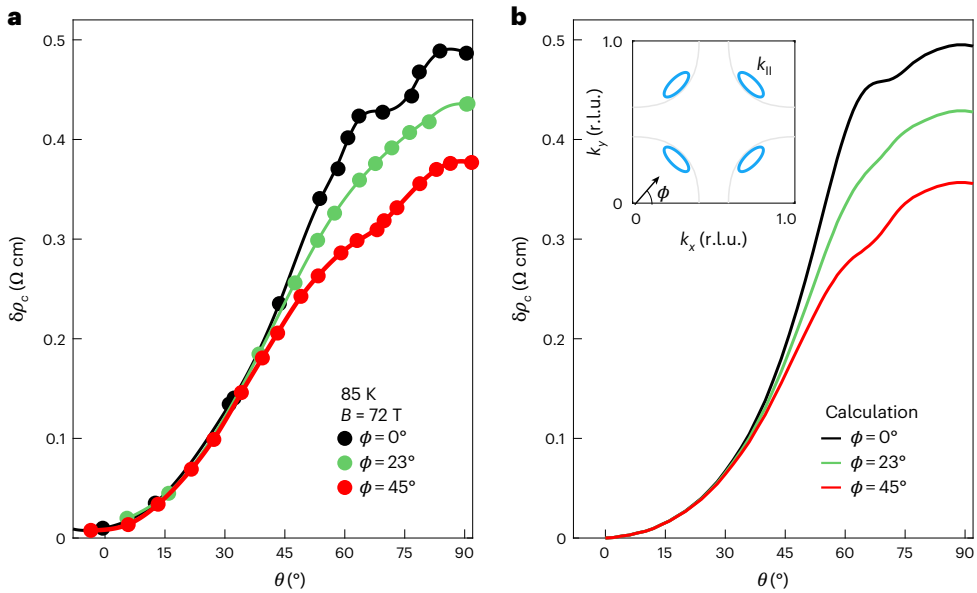

Fig. 2 | Comparison of measured angle-dependent magnetoresistivity with a Boltzmann transport model. a, Magnetoresistivity $\delta\rho_c = \rho_c(B) - \rho_c(0)$ at $B = 72$ T and 85 K as a function of θ for $\phi = 0°$, 23° and 45°. Full underlying data is shown in Extended Data Fig. 1. Solid lines are guides to the eye. **b**, Equivalent simulated $\delta\rho_c(\theta)$ (Methods). Inset, Fermi surface used for simulations. r.l.u. is the planar reciprocal lattice unit of Hg1201.

tilt, causing v_c to not only change around an orbit but also to change sign for an increasingly large fraction of the trajectory, yielding a smaller overall conductivity, or large magnetoresistivity. Experimentally, we find $\delta\rho_c \approx 0$ near $\theta = 0°$ and a large positive $\delta\rho_c$ at finite θ, which is consistent with the above description (Fig. 1e)[29]. Upon reaching the Yamaji angle, θ_{Yamaji}, all cyclotron orbits have the same cross-sectional area and the averaged velocity for all complete orbits vanishes[23]. As a result, the c-axis conductivity is fully suppressed in the clean limit, causing a large Yamaji peak in the polar-angle dependence of the magnetoresistivity. The Yamaji peak is attenuated and eventually disappears into the background with decreasing $\omega_c\tau$ because progressively fewer electrons are able to complete cyclotron orbits. The observed local maximum in $\delta\rho_c$ is indeed suppressed with decreasing magnetic field or increasing temperature, as shown in Fig. 1e,f. This local maximum is identified as the Yamaji peak.

The Yamaji peak, and its angular scale, θ_{Yamaji}, also determines the caliper Fermi radius, k_{cal}, of the Fermi pocket[24,25]. The value of k_{cal} is the maximum planar projection of the Fermi momentum along the azimuthal direction of the magnetic field, as depicted schematically for the example of an elliptical pocket in Fig. 1g. The Yamaji peak corresponds geometrically to when the tilted orbital trajectories on the Fermi surface span approximately three quarters of the c-axis reciprocal lattice unit, $c^* = 2\pi/c$, where $c = 9.5$ Å is the c-axis lattice parameter of Hg1201 (Fig. 1d). Therefore, the smaller k_{cal} is, the more the orbits need to be tilted, and the larger θ_{Yamaji} must be. For a Fermi surface with a circular or elliptical cross-section, this geometric consideration yields the exact relationship $\tan\theta_{Yamaji} = 3/4(c^*/2k_{cal})$ (see schematic inset of Fig. 1g and Methods)[23–25]. For Fermi surfaces that deviate from a perfect ellipse or have higher planar symmetry, this relationship is valid to leading order with a relatively weak ϕ-dependent modulation (see the example of a four-fold planar symmetry Fermi pocket in Extended Data Fig. 4)[30,31]. From the observed θ_{Yamaji} in Fig. 1g, we obtain $k_{cal} = 0.12$ Å^{-1} and 0.16 Å^{-1} for $\phi = 0°$ and 45°, respectively. These are substantially smaller than the Fermi momentum of approximately 0.7 Å^{-1} for the large Fermi surface expected from band structure calculations in Hg1201 (ref. 32,33).

The observation of the Yamaji peak in Hg1201 described above is evidence for a small Fermi-surface pocket, independent of fitting to a specific Fermi-surface model. As expected for a simply warped Fermi surface, the angle-dependent magnetoresistivity is relatively featureless when $\omega_c\tau < 1$ (green curve in Fig. 1e). However, the Yamaji peak becomes evident for the large $\omega_c\tau = 2.6$ achieved with $B = 72$ T (Methods). By comparison, the observed magnetoresistivity of lower-symmetry cuprates that have staggered copper-oxide planes, such as Nd-LSCO and $Tl_2Ba_2CuO_{6+\delta}$, have a rich angle-dependent structure even at small $\omega_c\tau \approx 0.2$ (ref. 21) and 0.5 (ref. 27), respectively. Interpreting this structure necessitated comparisons with detailed Boltzmann transport simulations for Fermi surfaces with higher-order warping terms[21,27].

Boltzmann transport simulation

Having established the existence of small Fermi pockets, we can gain more insight into the geometry of the Fermi surface in Hg1201 by comparing the magnetoresistivity with Boltzmann transport simulations[21,27,34]. A simple model Fermi surface that captures our observations has a planar cross-section comprising two sets of orthogonally oriented ellipses, depicted in the inset of Fig. 2b. Figure 2 shows a side-by-side comparison of measurements of $\delta\rho_c$ and simulations at three different azimuthal angles. The size and anisotropy of the pockets was fixed by the observed Yamaji angles such that the simulation employed only two adjustable parameters: $\omega_c\tau$, and the c-axis hopping amplitude t_c (see Methods for values). Figure 2 shows that the observed angle-dependent magnetoresistivity, including the magnitude and location of Yamaji peaks, was captured by the simulation.

A crucial observation is the strong azimuthal-angle dependence of the Yamaji peak shown in Fig. 2: a clear Yamaji peak for $\phi = 0°$ (black curves), its disappearance at the intermediate angle $\phi = 23°$ (green curves) and weak reappearance at $\phi = 45°$ (red curves). This can be understood from a superposition of magnetoconductivity of the two sets of orthogonal elliptical pockets. It is instructive to note that the Yamaji peak is, in fact, the first in an infinite series of peaks. Although strongly damped at larger angles, these peaks are periodic in $\tan\theta$ and are referred to as angle-dependent magnetoresistance oscillations (AMROs)[24,25]. When two or more pockets are present, the total conductance is the sum of their respective contributions, and their AMROs interfere (illustrated in Extended Data Fig. 5). The AMROs interfere constructively for the two sets of orthogonal pockets at $\phi = 0°$. At $\phi = 45°$, the AMRO is different for the two pockets, causing the

https://doi.org/10.1038/s41567-025-03032-2

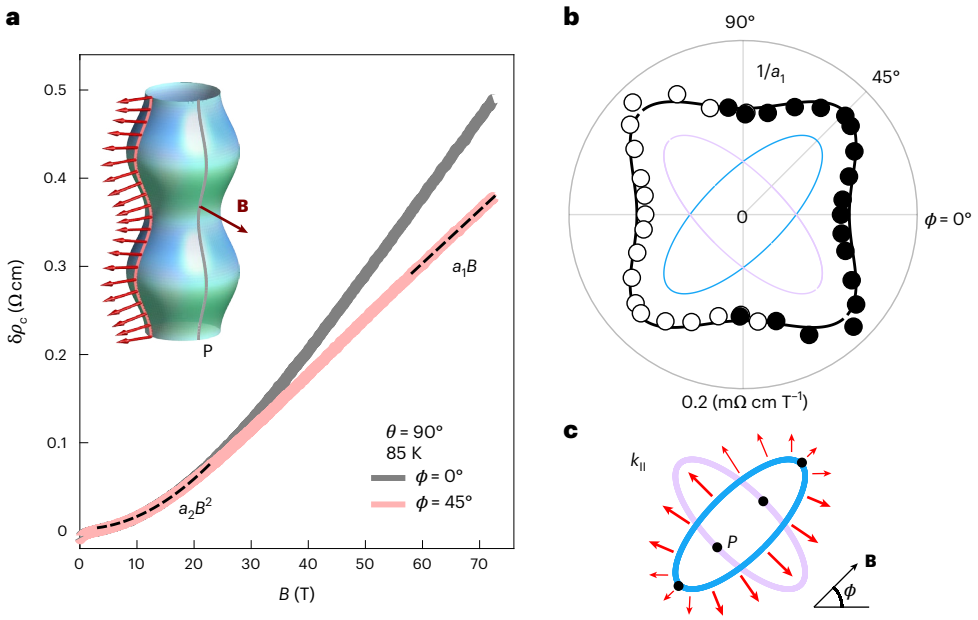

Fig. 3 | Magnetoresistivity for in-plane magnetic field. a, $\delta\rho_c = \rho_c(B) - \rho_c(0)$ for $\theta = 90°$. The magnetoresistivity $\delta\rho_c$ is linear at high field with slope $a_1(\phi)$ and quadratic at low field. The inset shows a schematic open orbit on the Fermi pocket. On the line marked P, $\mathbf{v}_\parallel \| \mathbf{B}$ such that quasiparticles do not experience a Lorentz force. **b**, Azimuthal-angle dependence of $1/a_1(\phi)$ (circles) extracted from fitting measured magnetoresistivity; see Extended Data Fig. 2 for underlying magnetoresistivity data. Open circles are mirrored from the measured data. The blue and purple lines are the calculated $1/a_1(\phi)$ of each of the two orthogonally oriented elliptical Fermi-surface cross-sections in our model. The solid black line is the sum of these two contributions. **c**, Planar elliptical cross-sections of the Fermi pockets superimposed to demonstrate the resulting anisotropy of $1/a_1(\phi)$. Red arrows represent $v_\parallel$ around one of the pockets. Black dots indicate points P on the Fermi surface which determine a_1 for the example of $\phi = 45°$.

constructive interference to be incomplete and yielding a smaller combined Yamaji peak. By contrast, at the intermediate angle of $\phi = 23°$, the two sets of orthogonal pockets happen to mostly interfere destructively, rendering the Yamaji peaks indiscernible in our experiment.

Magnetoresistivity for in-plane magnetic field

Further evidence for the Fermi-surface geometry can be found by considering the magnetoresistivity far from the Yamaji angle, when the magnetic field is oriented within the a–b plane ($\theta = 90°$). As shown in Fig. 3a, $\delta\rho_c$ has quadratic-in-field, then crosses over to linear-in-field behaviour ($\delta\rho_c = a_1 B$, where a_1 is the linear slope coefficient), with increasing magnetic field. The value of a_1 is ϕ dependent, as shown in Fig. 3b.

To understand this result, consider that, for a planar orientation of the magnetic field, the Lorentz force gives rise to open trajectories running along the c axis in momentum space, k_c, depicted schematically in the inset to Fig. 3a. The quasiparticle trajectories are periodic in the c-axis reciprocal lattice unit and the corresponding c-axis transit frequency for one period is $\omega_\perp = (ec/\hbar)|\mathbf{v}_\parallel \times \mathbf{B}|$, where $\mathbf{v}_\parallel$ is the planar component of the instantaneous velocity and $\hbar$ is the reduced Planck constant[25,35]. Warping causes v_c on the open trajectories to oscillate such that its average over a period is zero, resulting in the large magnetoresistivity. As expected for the Lorentz force, states with planar velocities that are predominantly transverse to the applied magnetic field experience a larger force and thus have larger $\omega_\perp$. At high magnetic fields, trajectories with $\omega_\perp \tau \gg 1$ are in the clean limit such that their time-delayed velocity correlations are zero and therefore no longer contribute to the overall conductivity.

However, the Lorentz force, and thus the $\omega_\perp$, goes to zero at points on the Fermi surface where the planar velocity is parallel to the magnetic field, labelled P in the inset of Fig. 3a. In the vicinity of P, the planar velocities are almost parallel to the applied field such that $\omega_\perp \tau$ remains small even as other trajectories have reached the clean limit. As a result, the states near P dominate the conductivity at high fields, and are responsible for the observed linear-in-field magnetoresistivity. The number of such states, and thus the magnitude of the slope, depends on the curvature of the Fermi surface at P (ref. 25).

In particular, the slope of the linear magnetoresistivity is obtained from the simple relationship $a_1(\phi) \propto v_\parallel(\phi)^2/R_\parallel(\phi)$, where $R_\parallel(\phi)$ and $v_\parallel(\phi)$ are, respectively, the in-plane radius of curvature and the Fermi velocity at P on the Fermi surface[36]. Note that the value of a_1 is independent of the scattering rate. The location of P on the Fermi surface is controlled by the orientation of the magnetic field, as depicted for one example in Fig. 3c. Therefore, measurements of a_1 as a function of ϕ effectively probe the planar cross-sectional geometry of the quasi-two-dimensional Fermi surface.

A number of conclusions, consistent with the Yamaji effect observations above, can be made from our measurements of the field in-plane magnetoresistivity. First, because the crossover to linear behaviour is due to points P where $\mathbf{v}_\parallel \| \mathbf{B}$, its observation for all ϕ spanning more than 180° azimuthal angular range (Extended Data Fig. 2) requires finite planar Fermi velocities along all azimuthal directions. As argued in ref. 35, this is a property of Fermi pockets and is not expected from the truncated Fermi arcs seen in photoemission[19]. The same argument precludes open Fermi-surface sheets, extended along k_c and one planar direction[25]. The presence of such Fermi sheets should cause strong two-fold in-plane anisotropy of magnetoresistivity, contrary to our observations shown in Fig. 3b. Finally, considering the two sets of elliptical Fermi pockets in our model, the inverse linear slopes calculated from the radius of curvature and planar velocities for each pocket are summed (because $\sigma_c \propto 1/a_1$) to yield the expected planar anisotropy. The result (black line) is in agreement with the measured $a_1(\phi)$, as shown in Fig. 3b (we have plotted the inverse of $a_1(\phi)$ for clarity), which thus confirms the geometry of the Fermi surface given by our model.

Discussion

The magnetoresistivity exhibiting a clear Yamaji peak is understood through the semiclassical evolution of the velocity under the Lorentz force acting on a quasi-two-dimensional Fermi-surface pocket.

Observation of the Yamaji peak in Hg1201 is thus evidence for the presence of small Fermi pockets in the normal state (above T_c) of Hg1201. Semiclassical simulations find that a Fermi surface comprising two sets of orthogonally oriented ellipses reproduces the magnetoresistivity data.

These results can be compared with previous Fermi-surface studies in Hg1201. The relationship to photoemission Fermi arcs present above T_c in other cuprates[15] is uncertain as neither arcs nor pockets have been reported in photoemission studies of Hg1201 thus far[37,38]. On the other hand, magnetic quantum oscillation measurements at temperatures well below T_c ($T \lesssim 4$ K) (refs. 39,40), revealed a small Fermi pocket with a frequency of $F = 860$ T at the hole doping studied here[12]. This is much larger than that of the high-temperature elliptical pockets reported here, which occupy an area equivalent to a quantum oscillation frequency of only $F = A\hbar/(2\pi e) = 360(50)$ T where A is the Fermi-surface planar cross-sectional area. Therefore, the low-temperature Fermi pocket is likely to result from the further reconstruction of the pseudogap Fermi surface with decreasing temperature and sufficiently large magnetic fields to suppress the superconductivity. Evidence of this reconstruction[8,11] include a change in sign of the Hall effect which occurs at $T \approx 20$ K in Hg1201 (ref. 12). We note that the low-temperature reconstructed Fermi surface in Hg1201, argued to be caused by charge-density-wave order[40–42], does not yield the angle-dependent magnetoresistivity reported here (Extended Data Fig. 6).

The small size of the Fermi pockets in the pseudogap state above T_c is contrary to expectations of a large Fermi surface from band structure calculations[32,37]. It therefore raises the question of its possible microscopic origin. So far, there is no evidence for conventional mechanisms producing pockets in Hg1201 above T_c, such as antiferromagnetic or charge-density-wave order, which involve translational symmetry breaking[7,8]. Neutron scattering in the pseudogap state of Hg1201 finds only short-range antiferromagnetic fluctuations with a spin gap of order 30 meV (ref. 43) and instantaneous correlation length of approximately 20 Å. Charge-density-wave correlations are also very short ranged (between 20 to 30 Å) and unaffected by applied magnetic field in the pseudogap state of Hg1201 (ref. 41).

Short-ranged correlations have been argued as potentially responsible for small Fermi pockets, particularly when the observed transport mean free path, λ, is comparable with the short-correlation lengths[21,44]. For Hg1201, such a scenario is precluded by the large value of $\omega_c\tau$. Using the relationship $\omega_c\tau = \lambda/\lambda_c$, where λ_c is the cyclotron radius, we determined $\lambda \approx 250$ Å in Hg1201 at 85 K, which is an order of magnitude larger than known correlation lengths of charge-density-wave or antiferromagnetic fluctuations above T_c.

Alternative proposals for the pseudogap state include those without broken translational symmetry (that is, $\mathbf{Q} = 0$ order)[45,46]. Although there have been experimental indications of $\mathbf{Q} = 0$ symmetry breaking across the pseudogap temperature T^* in Hg1201 (refs. 5,6), they cannot reconstruct the Fermi surface. The absence of any long-range order capable of reconstructing the Fermi surface calls into question the role of symmetry breaking as the cause of the pseudogap, and suggests the need for an unconventional mechanism[16–18]. The origins of the pseudogap of the cuprates must undoubtedly also explain the small pockets observed here.

Online content

Any methods, additional references, Nature Portfolio reporting summaries, source data, extended data, supplementary information, acknowledgements, peer review information; details of author contributions and competing interests; and statements of data and code availability are available at https://doi.org/10.1038/s41567-025-03032-2.

References

1. Keimer, B., Kivelson, S. A., Norman, M. R., Uchida, S. & Zaanen, J. From quantum matter to high-temperature superconductivity in copper oxides. *Nature* **518**, 179–186 (2015).
2. Xia, J. et al. Polar Kerr-effect measurements of the high-temperature $YBa_2Cu_3O_{6+x}$ superconductor: evidence for broken symmetry near the pseudogap temperature. *Phys. Rev. Lett.* **100**, 127002 (2008).
3. Shekhter, A. et al. Bounding the pseudogap with a line of phase transitions in $YBa_2Cu_3O_{6+\delta}$. *Nature* **498**, 75–77 (2013).
4. Zhao, L. et al. A global inversion-symmetry-broken phase inside the pseudogap region of $YBa_2Cu_3O_y$. *Nat. Phys.* **13**, 250–254 (2017).
5. Bourges, P., Bounoua, D. & Sidis, Y. Loop currents in quantum matter. *Comptes Rendus. Physique* **22**, 7–31 (2021).
6. Murayama, H. et al. Diagonal nematicity in the pseudogap phase of $HgBa_2CuO_{4+\delta}$. *Nat. Commun.* **10**, 3282 (2019).
7. Sebastian, S. E., Harrison, N. & Lonzarich, G. G. Towards resolution of the Fermi surface in underdoped high-T_c superconductors. *Rep. Prog. Phys.* **75**, 102501 (2012).
8. Proust, C. & Taillefer, L. The remarkable underlying ground states of cuprate superconductors. *Annu. Rev. Condens. Matter Phys* **10**, 409–429 (2019).
9. Ramshaw, B. J. et al. Broken rotational symmetry on the Fermi surface of a high-T_c superconductor. *npj Quantum Mater.* **2**, 8 (2017).
10. Gerber, S. et al. Three-dimensional charge density wave order in $YBa_2Cu_3O_{6.67}$ at high magnetic fields. *Science* **350**, 949–952 (2015).
11. LeBoeuf, D. et al. Electron pockets in the Fermi surface of hole-doped high-T_c superconductors. *Nature* **450**, 533–536 (2007).
12. Chan, M. K. et al. Extent of Fermi-surface reconstruction in the high-temperature superconductor $HgBa_2CuO_{4+\delta}$. *Proc. Natl Acad. Sci. USA* **117**, 9782–9786 (2020).
13. Kunisada, S. et al. Observation of small Fermi pockets protected by clean CuO_2 sheets of a high-T_c superconductor. *Science* **369**, 833–838 (2020).
14. Norman, M. R. et al. Destruction of the Fermi surface in underdoped high-T_c superconductors. *Nature* **392**, 157–160 (1998).
15. Sobota, J. A., He, Y. & Shen, Z.-X. Angle-resolved photoemission studies of quantum materials. *Rev. Mod. Phys.* **93**, 025006 (2021).
16. Kaul, R. K., Kolezhuk, A., Levin, M., Sachdev, S. & Senthil, T. Hole dynamics in an antiferromagnet across a deconfined quantum critical point. *Phys. Rev. B* **75**, 235122 (2007).
17. Rice, T. M., Yang, K.-Y. & Zhang, F. C. A phenomenological theory of the anomalous pseudogap phase in underdoped cuprates. *Rep. Prog. Phys.* **75**, 016502 (2011).
18. Mascot, E. et al. Electronic spectra with paramagnon fractionalization in the single-band Hubbard model. *Phys. Rev. B* **105**, 075146 (2022).
19. Reber, T. J. et al. The origin and non-quasiparticle nature of Fermi arcs in $Bi_2Sr_2CaCu_2O_{8+\delta}$. *Nat. Phys.* **8**, 606–610 (2012).
20. Norman, M. R., Kanigel, A., Randeria, M., Chatterjee, U. & Campuzano, J. C. Modeling the Fermi arc in underdoped cuprates. *Phys. Rev. B* **76**, 174501 (2007).
21. Fang, Y. et al. Fermi surface transformation at the pseudogap critical point of a cuprate superconductor. *Nat. Phys.* **18**, 558–564 (2022).
22. Musser, S., Chowdhury, D., Lee, P. A. & Senthil, T. Interpreting angle-dependent magnetoresistance in layered materials: application to cuprates. *Phys. Rev. B* **105**, 125105 (2022).
23. Yamaji, K. On the angle dependence of the magnetoresistance in quasi-two-dimensional organic superconductors. *J. Phys. Soc. Jpn.* **58**, 1520–1523 (1989).
24. Singleton, J. Studies of quasi-two-dimensional organic conductors based on BEDT-TTF using high magnetic fields. *Rep. Prog. Phys* **63**, 1111–1207 (2000).

25. Kartsovnik, M. V. High magnetic fields: a tool for studying electronic properties of layered organic metals. *Chem. Rev.* **104**, 5737–5782 (2004).
26. Shoenberg, D. *Magnetic Oscillations in Metals* (Cambridge Univ. Press, 1984).
27. Hussey, N. E., Abdel-Jawad, M., Carrington, A., Mackenzie, A. P. & Balicas, L. A coherent three-dimensional Fermi surface in a high-transition-temperature superconductor. *Nature* **425**, 814–817 (2003).
28. Putilin, S. N., Antipov, E. V., Chmaissem, O. & Marezio, M. Superconductivity at 94 K in $HgBa_2CuO_{4+\delta}$. *Nature* **362**, 226–228 (1993).
29. Lewin, S. K. & Analytis, J. G. Angle-dependent magnetoresistance as a probe of Fermi surface warping in $HgBa_2CuO_{4+\delta}$. *Phys. Rev. B* **98**, 075116 (2018).
30. Grigoriev, P. D. Angular dependence of the Fermi surface cross-section area and magnetoresistance in quasi-two-dimensional metals. *Phys. Rev. B* **81**, 205122 (2010).
31. Nam, M. S., Blundell, S. J., Ardavan, A., Symington, J. A. & Singleton, J. Fermi surface shape and angle-dependent magnetoresistance oscillations. *J. Phys. Condens. Matter* **13**, 2271–2279 (2001).
32. Das, T. Q=0 collective modes originating from the low-lying Hg-O band in superconducting $HgBa_2CuO_{4+\delta}$. *Phys. Rev. B* **86**, 054518 (2012).
33. Sakakibara, H., Usui, H., Kuroki, K., Arita, R. & Aoki, H. Origin of the material dependence of T_c in the single-layered cuprates. *Phys. Rev. B* **85**, 064501 (2012).
34. Goddard, P. A. et al. Angle-dependent magnetoresistance of the layered organic superconductor κ– $(ET)_2Cu(NCS)_2$: simulation and experiment. *Phys. Rev. B* **69**, 174509 (2004).
35. Smith, M. F. & McKenzie, R. H. Fermi surface of underdoped cuprate superconductors from interlayer magnetoresistance: closed pockets versus open arcs. *Phys. Rev. B* **82**, 172510 (2010).
36. Lebed, A. G. & Bagmet, N. N. Nonanalytical magnetoresistance, the third angular effect, and a method to investigate Fermi surfaces in quasi-two-dimensional conductors. *Phys. Rev. B* **55**, R8654–R8657 (1997).
37. Vishik, I. M. et al. Angle-resolved photoemission spectroscopy study of $HgBa_2CuO_{4+\delta}$. *Phys. Rev. B* **89**, 195141 (2014).
38. Sreedhar, S. A. et al. Three interaction energy scales in the single-layer high-T_c cuprate $HgBa_2CuO_{4+\delta}$. *Phys. Rev. B* **102**, 205109 (2020).
39. Barišić, N. et al. Universal quantum oscillations in the underdoped cuprate superconductors. *Nat. Phys.* **9**, 761–764 (2013).
40. Chan, M. K. et al. Single reconstructed Fermi surface pocket in an underdoped single-layer cuprate superconductor. *Nat. Commun.* **7**, 12244 (2016).
41. Tabis, W. et al. Synchrotron x-ray scattering study of charge-density-wave order in $HgBa_2CuO_{4+\delta}$. *Phys. Rev. B* **96**, 134510 (2017).
42. Comin, R. & Damascelli, A. Resonant X-ray scattering studies of charge order in cuprates. *Annu. Rev. Condens. Matter Phys.* **7**, 369–405 (2016).
43. Chan, M. K. et al. Commensurate antiferromagnetic excitations as a signature of the pseudogap in the tetragonal high-T_c cuprate $HgBa_2CuO_{4+\delta}$. *Nat. Commun.* **7**, 10819 (2016).
44. Gannot, Y., Ramshaw, B. J. & Kivelson, S. A. Fermi surface reconstruction by a charge density wave with finite correlation length. *Phys. Rev. B* **100**, 045128 (2019).
45. Varma, C. M. Non-Fermi-liquid states and pairing instability of a general model of copper oxide metals. *Phys. Rev. B* **55**, 14554–14580 (1997).
46. Kivelson, S. A., Fradkin, E. & Emery, V. J. Electronic liquid-crystal phases of a doped Mott insulator. *Nature* **393**, 550–553 (1998).
47. Yamamoto, A., Hu, W.-Z. & Tajima, S. Thermoelectric power and resistivity of $HgBa_2CuO_{4+\delta}$ over a wide doping range. *Phys. Rev. B* **63**, 024504 (2000).

Methods

Sample preparation

Hg1201 single crystals were grown using an encapsulated self-flux method[48]. Samples from the same batch were used for a previous study showing quantum oscillations[12] at low temperatures. The measured sample was underdoped with $p = 0.1$ and $T_c = 74$ K. Newly synthesized crystals were heat treated at 450 °C in flowing nitrogen for one month to achieve the desired hole doping. The stated hole concentration of the sample was determined by relating T_c to a phenomenological Seebeck coefficient scale[47] consistent with previous works[12,48].

Pulsed-field measurements

High-magnetic-field measurements were performed at the Pulsed-Field Facility of the National High Magnetic Field Laboratory at Los Alamos National Laboratory. Measurements were made with the 75 T duplex magnet whose pulse profile is shown in Extended Data Fig. 3c. Extended Data Fig. 3a,b demonstrates fidelity of the data collected during the magnetic field pulses. The values of ρ_c at a particular B were obtained from averaging the measured values in the range $B \pm 0.5$ T.

Calculation of resistivity

The conductivity of a metal is given by the Kubo formula

$$\sigma_{\alpha\beta}(\omega) = \frac{1}{\mathrm{i}\omega}\int \mathrm{d}t\, \mathrm{e}^{\mathrm{i}\omega t}\, \langle\langle j_\alpha(t)\, j_\beta(0)\rangle\rangle, \tag{1}$$

where $\langle\langle \ldots \rangle\rangle$ are the thermodynamic and quantum averages. The static conductivity was obtained by taking the zero-frequency limit $\omega \to 0$. In the semiclassical limit, the Kubo formula reduces to the average of the velocity over all possible classical trajectories

$$\sigma_{\alpha\beta} = 2e^2\,\frac{N_{2D}}{(2\pi)^2}\,\omega_c\cos\theta \int_{-\frac{\pi}{c}}^{\frac{\pi}{c}} \frac{\mathrm{d}k_{c0}}{2\pi}\int \mathrm{d}t'\int_0^\infty \mathrm{d}t\; v_\alpha(t+t')\, v_\beta(t')\, \mathrm{e}^{-t/\tau}, \tag{2}$$

where N_{2D} is the average two-dimensional density of states at the chemical potential. The quasiparticle current is given by the product of electron charge and velocity $j_\alpha = e v_\alpha$. The factor of two accounts for the two spin components. $\omega_c = eB/m^\star$ is the cyclotron frequency. The value $m^\star$ is the in-plane effective mass, assuming an in-plane parabolic approximation to the dispersion. Integration over t' accounts for all possible starting points on a given trajectory. The value k_{c0} is the central c-axis momentum of each orbit, and its integration accounts for all orbits with different vertical offsets along the c-axis direction of momentum space. In addition, $v(t)$ is the instantaneous velocity of a quasiparticle as its momentum-space location on the Fermi surface evolves in time under a Lorentz force. The exponent accounts for scattering effects within the relaxation-time approximation. We first considered the case of a warped cylindrical Fermi surface (that is, with a circular cross-section in the a–b plane). We then extended it to a Fermi surface with an elliptical cross-section. The dispersion of a warped cylindrical Fermi surface is

$$\epsilon(\mathbf{k}) = \frac{\mathbf{k}_\parallel^2}{2m^\star} - 2\,t_c\cos(k_c\,c), \tag{3}$$

where $\mathbf{k}_\parallel$ is the in-plane component of the momentum, k_c is the c-axis component of the momentum and c is the c-axis lattice spacing. The second term represents the simplest form of warping along c, lowest-harmonic sinusoidal. The c-axis hopping t_c is small, in the sense that the mass m_c associated with the the c-axis dispersion, $m_c = \hbar^2/(t_c\,c^2)$ is much larger than the in-plane mass, $m^\star/m_c \ll 1$. Such a weak c-axis hopping is responsible for the weak warping of the otherwise perfectly cylindrical Fermi surface.

Equation (2) is more easily evaluated by converting the integration over time variables, t and t', to azimuthal angles of the electron momentum, ψ and ψ', on a closed orbit. This change in variable is possible because ψ is a monotonic function of t. Upon implementing the change in variable, we obtain

$$\sigma_{\alpha\beta} = 2e^2\,\frac{N_{2D}}{(2\pi)^2}\,\omega_c\cos\theta \int_{-\frac{\pi}{c}}^{\frac{\pi}{c}} \mathrm{d}k_{c0}\int_0^{2\pi}\frac{\mathrm{d}\psi'}{\Omega(\psi')}\int_{\psi'}^{\infty}\frac{\mathrm{d}\psi}{\Omega(\psi)} \\ v_\alpha(\psi+\psi')\, v_\beta(\psi')\,\exp\left\{-\frac{1}{\tau}\int_{\psi'}^{\psi}\frac{\mathrm{d}\psi''}{\Omega(\psi'')}\right\}, \tag{4}$$

where $\Omega(\psi)$ is the Jacobian of the variable change from time t to azimuthal angle ψ: $\Omega(\psi) = \mathrm{d}\psi(t)/\mathrm{d}t$. The Jacobian is $\Omega(\psi) = (\mathrm{d}\psi/\mathrm{d}\mathbf{k}_\parallel)\,(\mathrm{d}\mathbf{k}_\parallel/\mathrm{d}t)$, where $\mathbf{k}_\parallel$ is the in-plane projection of the electron momentum. The first factor is purely geometric and connects the azimuthal angle ψ to the in-plane momentum $\mathbf{k}_\parallel$. The second factor is equal to the force acting on the electron under classical evolution, $\mathrm{d}k/\mathrm{d}t = F$. For a Lorentz force, $\mathbf{F} = e\mathbf{B}\times\mathbf{v}$, we obtain

$$\Omega(\psi) = \frac{e}{k_\parallel^2}\left[B_c\;(\mathbf{k}_\parallel\cdot\mathbf{v}_\parallel) - v_c\;(\mathbf{k}_\parallel\cdot\mathbf{B}_\parallel)\right], \tag{5}$$

where $k_\parallel = |\mathbf{k}_\parallel|$ and $\mathbf{v}_\parallel$ is the in-plane component of the velocity. The variables B_c and v_c are the c-axis components of magnetic field and instantaneous velocity, respectively. The second term vanishes for zero warping because $v_c \to 0$ when $t_c \to 0$. At finite but small warping, the second term is smaller than the first by a small factor of order $m^\star/m_c$. To leading order of $m^\star/m_c$, we can ignore the second term such that the Jacobian depends only on the in-plane dispersion, as commonly done[25,29]. For a circular in-plane cross-section, equation (2), the Jacobian $\Omega(\psi)$ is independent of ψ and is given by $\Omega = \omega_c\cos(\theta)$.

For an elliptical pocket, the c-axis warping term of the dispersion in equation (3) is unchanged, whereas the planar term becomes

$$\epsilon_\parallel(\mathbf{k}_\parallel) = \frac{k_x^2}{2m_x} + \frac{k_y^2}{2m_y}, \tag{6}$$

where k_x and k_y are components of the in-plane momentum along the major and minor axis of the elliptical pocket. For such an elliptical pocket, the Jacobian is given by

$$\Omega(\psi) = \omega_c\cos\theta\;\frac{m^\star\left(\frac{k_x^2}{m_x}+\frac{k_y^2}{m_y}\right)}{k_x^2+k_y^2} = \omega_c\cos\theta\; m^\star\left(\frac{\cos^2\psi}{m_x}+\frac{\sin^2\psi}{m_y}\right), \tag{7}$$

Also for an elliptical pocket, both the cyclotron mass $m^* = (1/2\pi)\,\mathrm{d}A/\mathrm{d}\epsilon$ (where A is the area of the Fermi surface) and the density of states mass $m^* = \mathrm{d}N/\mathrm{d}\epsilon$ (where N is the total number of states enclosed by the Fermi surface) are equal to each other, $m^\star = \sqrt{m_x m_y}$. With this, the two-dimensional density of states per spin component is $N_{2D} = m^*/2\pi\hbar^2$.

In this approximation, where the Jacobian is independent of k_c, the integral over k_{c0} in equation (4) can be done analytically[22]. To do so, we first point out that, for an electron moving on a given orbit crossing the vertical axis at k_{c0}, there is a well-defined relationship between its c-axis momentum component $k_c(\psi)$ and its planar momentum $\mathbf{k}_\parallel(\psi)$. Again, considering the limit of small $m^\star/m_c$, this relationship is[25]

$$k_c(\psi) = k_{c0} + K_H(\psi)\tan\theta \qquad \text{where} \qquad K_H(\psi) = k_\parallel(\psi)\cos(\psi-\phi). \tag{8}$$

where $K_H(\psi)$ is the planar projection of the momentum $\mathbf{k}_\parallel$ on the azimuthal plane of the applied magnetic field at angle ϕ and θ is the polar angle of the applied magnetic field.

https://doi.org/10.1038/s41567-025-03032-2

As an electron traverses an orbit, $k_c(\psi)$ is a periodic function of ψ, between maximum value $k_{c,max}$ and minimum value $k_{c,min}$. Similarly, the extent of the orbit in the a–b plane is also finite, and is referred to as the caliper radius k_{cal}

$$k_{cal} = \frac{1}{2}\left\{\max_{\psi} - \min_{\psi}\right\} K_H(\psi). \tag{9}$$

It is easy to show[49] that, for an ellipse with semimajor and semiminor axes a and b, respectively, rotated by an angle γ,

$$k_{cal} = \sqrt{a^2\cos\{\phi-\gamma\}^2 + b^2\sin\{\phi-\gamma\}^2}. \tag{10}$$

We now consider the c-axis conductivity starting from equation (4). To leading order in m^*/m_e, the only dependence on k_{c0} in equation (4) comes from the dependence of $v_c(\psi)$ because it vanishes in the limit of zero warping. Specifically, $v_c(\psi)$ is entirely determined by the warping term in equation (3),

$$v_c(\psi) = \frac{2ct_c}{\hbar}\ \sin[c\,k_c(\psi)] = \frac{2ct_c}{\hbar}\ \sin\left[c\,k_{c0} + cK_H(\psi)\tan\theta\right], \tag{11}$$

where, after the second equality sign, we substituted equation (8) to express $k_c(\psi)$ in terms of $k_{||}(\psi)$.

Integrating the product of velocities in equation (4) over k_{c0} gives

$$\begin{aligned}
&\int_{-\frac{\pi}{c}}^{\frac{\pi}{c}} \mathrm{d}k_{c0}\ v_c(\psi)\,v_c(\psi') \\
&= \left(\tfrac{2ct_c}{\hbar}\right)^2 \int_{-\frac{\pi}{c}}^{\frac{\pi}{c}} \mathrm{d}k_{c0}\ \sin\left(c\,k_{c0} + cK_H(\psi)\tan\theta\right)\sin\left(c\,k_{c0} + cK_H(\psi')\tan\theta\right) \\
&= \tfrac{\pi}{c}\left(\tfrac{2ct_c}{\hbar}\right)^2 \cos\left(\tan\theta\,[cK_H(\psi) - cK_H(\psi')]\right)
\end{aligned} \tag{12}$$

Finally, we arrive at the following representation of c-axis conductivity

$$\begin{aligned}
\sigma_c = 2e^2\,\tfrac{N_{2D}}{(2\pi)^2}\,\omega_c\cos(\theta)\,\tfrac{\pi}{c}\left(\tfrac{2ct_c}{\hbar}\right)^2 \int_0^{2\pi}\tfrac{\mathrm{d}\psi'}{\Omega(\psi')}\int_{\psi'}^{\infty}\tfrac{\mathrm{d}\psi}{\Omega(\psi)}\ \exp\left\{-\tfrac{1}{\tau}\int_{\psi'}^{\psi}\tfrac{\mathrm{d}\psi''}{\Omega(\psi'')}\right\} \\
\times\cos\left[(cK_H(\psi) - cK_H(\psi'))\tan\theta\right],
\end{aligned} \tag{13}$$

where $cK_H(\psi) - cK_H(\psi')$ is a periodic function of ψ and ψ' with maximum and minimum values of $\pm\, c\,2k_{cal}$, respectively. In the clean limit, $\omega_c\tau \gg 1$, the argument of the integral is a periodic function of $\tan\theta\,[\,cK_H(\psi) - cK_H(\psi')]$. Therefore, upon integrating over ψ and ψ', the c-axis conductivity σ_c is a periodic function of the amplitude of the expression under the cosine. In other words, the minimum of σ_c is periodic in $c\,k_{cal}(\phi)\tan\theta$. In particular, the minimum of this periodic function defines the set of Yamaji angles[23]

$$c\,k_{cal}(\phi)\tan[\theta_{Yamaji}(\phi)] = \frac{3}{4}\pi + n\pi \qquad n = 0, 1, 2, \ldots, \infty. \tag{14}$$

Although this expression for the Yamaji angle has been derived analytically for an elliptical pocket, it has a purely geometric meaning. In particular, we remind the reader that $2k_{cal}\tan\theta$ is the vertical extent of the orbit. The first Yamaji angle corresponds to when the vertical extent of the orbit is equal to half of the distance from the belly of the first Brillouin zone to the neck of the next zone[23]. Larger θ_{Yamaji} corresponds to a smaller k_{cal}.

The c-axis resistivity is determined by inverting the conductivity $\rho_c \approx 1/\sigma_c$. For simulations, the conductivity contributions from each pocket were summed before inverting the total to obtain the resistivity.

Table 1 | Fermi-surface parameters

a (Å^{-1})	a/b	$\omega_c\tau$	t_c (meV)
0.164±0.03	2.6	2.6±0.2	0.34±0.02

The value a is the major axis radius of the elliptical cross-section of the Fermi pocket and a/b is the ratio between major and minor axis radii, or aspect ratio.

As described below, the Yamaji effect constrains the size and geometry of the Fermi pockets. After assuming a simple Fermi-surface model comprising four elliptical cross-sections at each of the nodes, the only additional parameters for our simulations were $\omega_c\tau$ and t_c. The value of $\omega_c\tau$ controls the size of the Yamaji peaks (Fig. 2a,b) and the magnetoresistivity $\delta\rho_c$. The c-axis hopping t_c controls the overall magnitude of the conductivity. The calculated conductivity is the sum of that from four pockets. Boltzmann simulations were only compared with the magnetoresistivity $\delta\rho_c$. As was found in other underdoped cuprates, the observed $\rho_c(0)$ was large and not captured by Boltzmann transport calculations[21]. This discrepancy is attributed to incoherent contributions whose origin is unknown.

The resultant parameters for the model Fermi surface are given in Table 1 below.

Determination of $\omega_c\tau$

Within our model, the value of $\omega_c\tau = 2.6 \pm 0.2$ was obtained by comparing our simulations with the prominence of the Yamaji peak for $\phi = 0°$, as shown in Extended Data Fig. 7. Using the same $\omega_c\tau$, simulations of all other curves with our model Fermi surface reproduced data shown in Figs. 2 and 3. For comparison, quantum oscillation measurements in the low-temperature Fermi surface reconstructed phase of Hg1201 at 2 K yielded $\omega_c\tau \approx 0.5$ (ref. 40). The effective scattering rate obtained from quantum oscillations is commonly substantially larger than that from magnetoresistivity analysis due to the former's sensitivity to large scale inhomogeneities[25]. A similar discrepancy is found in comparing $\omega_c\tau$ obtained from quantum oscillations and cyclotron resonance experiments[50]. It has also been argued that the charge-density-wave responsible for the small pockets seen with quantum oscillations might be short ranged[40], which suppresses $\omega_c\tau$.

The transport mean free path $\lambda \approx 250$ Å in Hg1201 was estimated from $\omega_c\tau$ in the main text. The value of λ can also be estimated, independently of a specific Fermi-surface model, from the observed crossover from quadratic to linear in-field magnetoresistivity when $\theta = 90°$. The crossover occurs when $\langle\omega_\perp\rangle\tau \approx 1$ or $\lambda \approx \hbar/(eBc)$ (ref. 51). The value $\langle\omega_\perp\rangle$ is the average c-axis transit frequency of all trajectories. Taking an approximate average crossover field of 25 T (Extended Data Fig. 2) yielded $\lambda \approx 280$ Å, which is in rather good agreement with that determined with $\omega_c\tau$. This is also additional confirmation, independent of modelling, that $B = 72$ T is sufficient to reach the high field regime necessary to observe the Yamaji effect.

We estimated $\omega_c\tau = (eB/m^*)\tau \approx 0.2$ for the angular-dependent magnetoresistivity study of Nd-LSCO (ref. 21) by using their quoted scattering rate of $1/\tau = 23$ ps^{-1}, $B = 45$ T and assuming that $m^* = 2m_e$, where m_e is the bare electron mass. The value of m^* was determined based on the Sommerfeld coefficient for electronic specific heat measured on similarly doped Nd-LSCO samples[52]. Ref. 21 notes that the cyclotron length in their measurements is $\lambda_c \approx 200$ Å, which yields a mean free path of $\lambda \approx 40$ Å.

Fermi pocket size and geometry

The measured Yamaji angles determine the size and ellipticity of the Fermi-surface pockets by means of equation (14). From Fig. 1g, we determined $\theta_{Yamaji}(\phi = 0°) = 63.5 \pm 2°$ and $\theta_{Yamaji}(\phi = 45°) = 56.5 \pm 3.5°$, corresponding to $k_{cal}(\phi = 0°) = 0.124 \pm 0.01$ Å^{-1} and $k_{cal}(\phi = 45°) = 0.164 \pm 0.03$ Å^{-1}. The latter corresponds to the major axis radius a, and the former permits a determination of the aspect ratio between major and

minor axis radii $a/b = 2.6$ using equation (10). The enclosed area of each pocket was $A = \pi ab$, which comes out to be approximately 1.3% of the area of the in-plane crystallographic Brillouin zone given by $(2\pi/3.9\ \text{Å})^2$. The measured linear slope of magnetoresistivity with field applied within the a–b plane also determines the Fermi pocket geometry by means of the relationship $a_1(\phi) \propto v_{\parallel}(\phi)^2/R_{\parallel}(\phi)$ (ref. 36) evaluated at the points P on the Fermi surface as shown in Fig. 3c. The radius of curvature for each ellipse is given by $R_{\parallel} = a^2b^2(k_x^2/a^4 + k_y^2/b^4)^{3/2}$, where k_x and k_y are the Fermi momenta at P. Point P moves around the Fermi pocket as the azimuthal orientation of the magnetic field ϕ is varied.

Data availability

Data that support the findings of this study are provided in the Extended Data figures. Source data are provided with this paper.

References

48. Zhao, X. et al. Crystal growth and characterization of the model high-temperature superconductor $HgBa_2CuO_{4+\delta}$. *Adv. Mater.* **18**, 3243–3247 (2006).
49. House, A. A. et al. Oscillatory magnetoresistance in the charge-transfer salt β''-BEDT-TTF_2AuBr_2 in magnetic fields up to 60 T: evidence for field-induced Fermi-surface reconstruction. *Phys. Rev. B* **53**, 9127–9136 (1996).
50. Hill, S. Semiclassical description of cyclotron resonance in quasi-two-dimensional organic conductors: theory and experiment. *Phys. Rev. B* **55**, 4931–4940 (1997).
51. Schofield, A. J. & Cooper, J. R. Quasilinear magnetoresistance in an almost two-dimensional band structure. *Phys. Rev. B* **62**, 10779–10784 (2000).
52. Michon, B. et al. Thermodynamic signatures of quantum criticality in cuprate superconductors. *Nature* **567**, 218–222 (2019).

Acknowledgements

We thank M. R. Norman and S. Sachdev for comments on the manuscript. The high-magnetic-field measurements and sample preparation were supported by the US Department of Energy BES 'Science of 100T' grant. The National High Magnetic Field Laboratory Pulsed-Field Facility is funded under the National Science Foundation Cooperative Agreement no. DMR-2128556, by the State of Florida and the US Department of Energy. M.K.C. acknowledges support from LDRD 20210320ER for calculations of electrical transport in unconventional superconductors. M.K.C. acknowledges support from the National Science Foundation IR/D programme for research performed while serving at the National Science Foundation, and from the dedicated staff. Any opinion, findings and conclusions or recommendations expressed in this material are those of the author(s) and do not necessarily reflect the views of the National Science Foundation.

Author contributions

M.K.C., K.A.S., O.E.A.-V. and N.H. developed the equipment and performed the pulsed-field measurements. M.K.C. and E.D.B synthesized the samples. M.K.C., K.A.S. and N.H. analysed and modelled the data. M.K.C., A.S. and N.H. interpreted the results and wrote the manuscript with critical input and review from all authors.

Competing interests

The authors declare no competing interests.

Additional information

Extended data is available for this paper at https://doi.org/10.1038/s41567-025-03032-2.

Supplementary information The online version contains supplementary material available at https://doi.org/10.1038/s41567-025-03032-2.

Correspondence and requests for materials should be addressed to Mun K. Chan.

Peer review information *Nature Physics* thanks Sylvia Lewin and the other, anonymous, reviewer(s) for their contribution to the peer review of this work.

https://doi.org/10.1038/s41567-025-03032-2

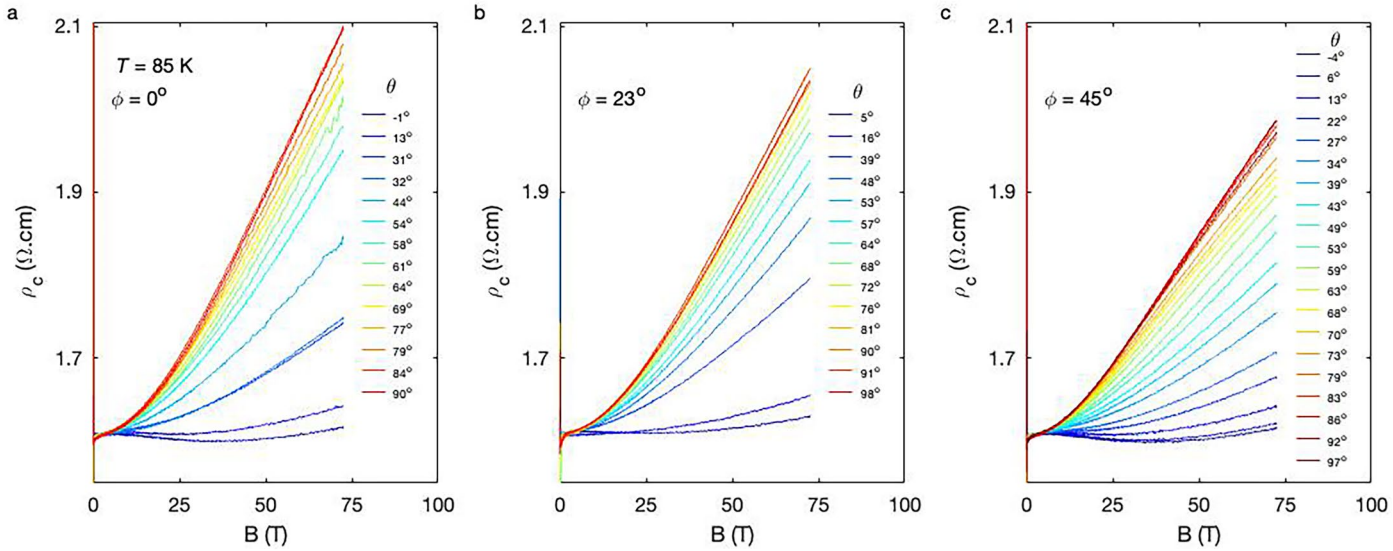

Extended Data Fig. 1 | θ dependence of magnetoresistivity. Magnetoresistivity field sweeps underlying the θ dependence plots in Figs. 1 and 2. **a**–**c** show magnetoresistivity for the magnetic field tilted into $\phi = 0^{\circ}$, 23°, and 45° respectively. $T = 85$ K.

https://doi.org/10.1038/s41567-025-03032-2

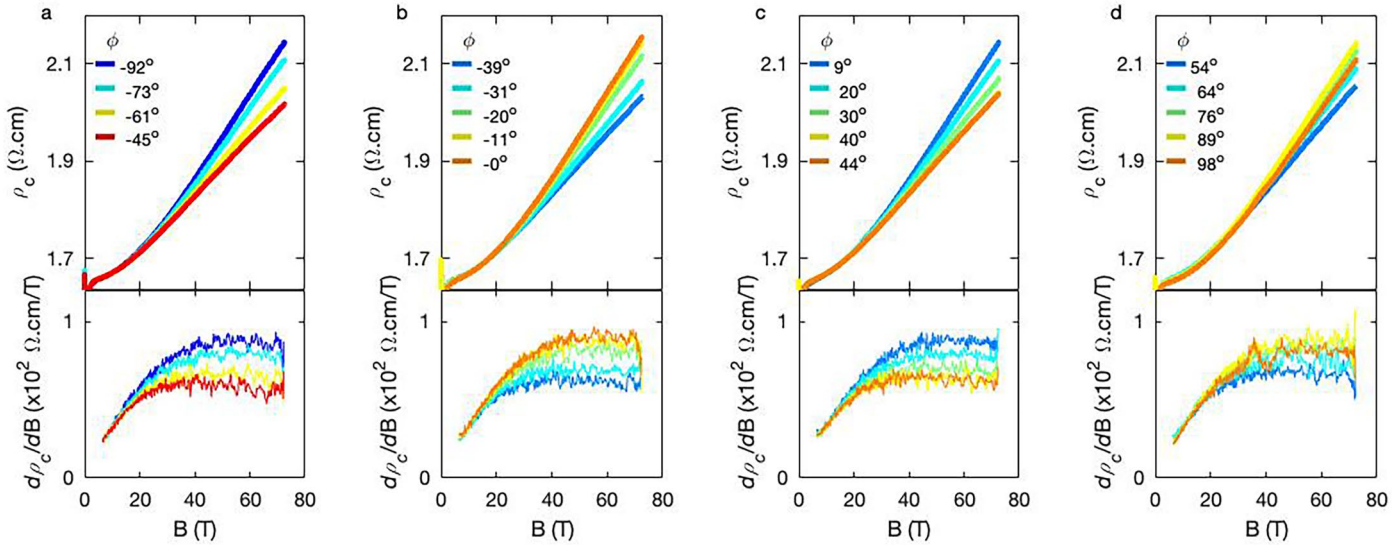

Extended Data Fig. 2 | ϕ dependence of magnetoresistivity. a–d, Magnetoresistivity field sweeps underlying the ϕ dependence plots in Fig. 3b, covering approximately 180° angular range. $\theta = 90°$ for all curves, corresponding to magnetic field applied in the plane. Lower panels are the derivative with respect to field, showing a crossover to linear magnetoresistance in all curves. $T = 85$ K.

https://doi.org/10.1038/s41567-025-03032-2

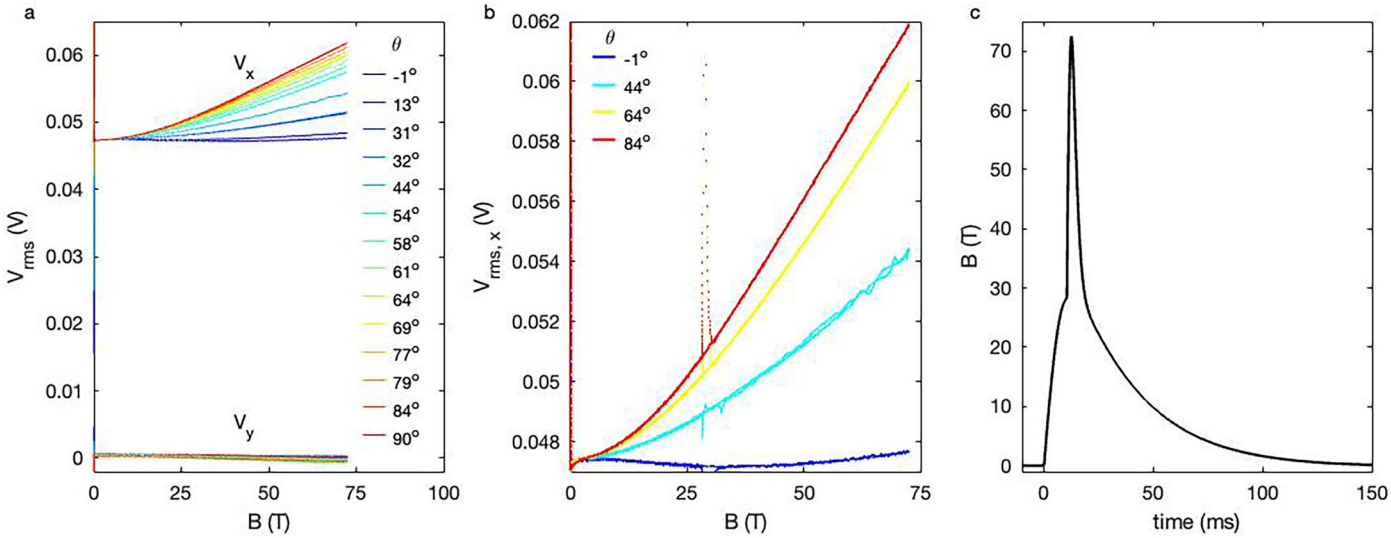

Extended Data Fig. 3 | Fidelity of pulsed magnetic field measurements. **a**, Measured V_x and V_y of the lock-in voltage corresponding to θ dependence of magnetoresistance at $\phi = 0^\circ$. The out-of-phase component V_y is much smaller than the in-phase component V_x of the detected voltage. **b**, Representative field dependence of measured voltage comparing up (dots) and down (line) sweeps of the pulsed field. The two fall on top of each other except for a large spike starting around B ≈ 25 T on the upsweep due to the firing of the insert. Only down sweep data were analyzed and presented in the main text. **c**, Pulsed field profile of the 75 Tesla Duplex magnet.

https://doi.org/10.1038/s41567-025-03032-2

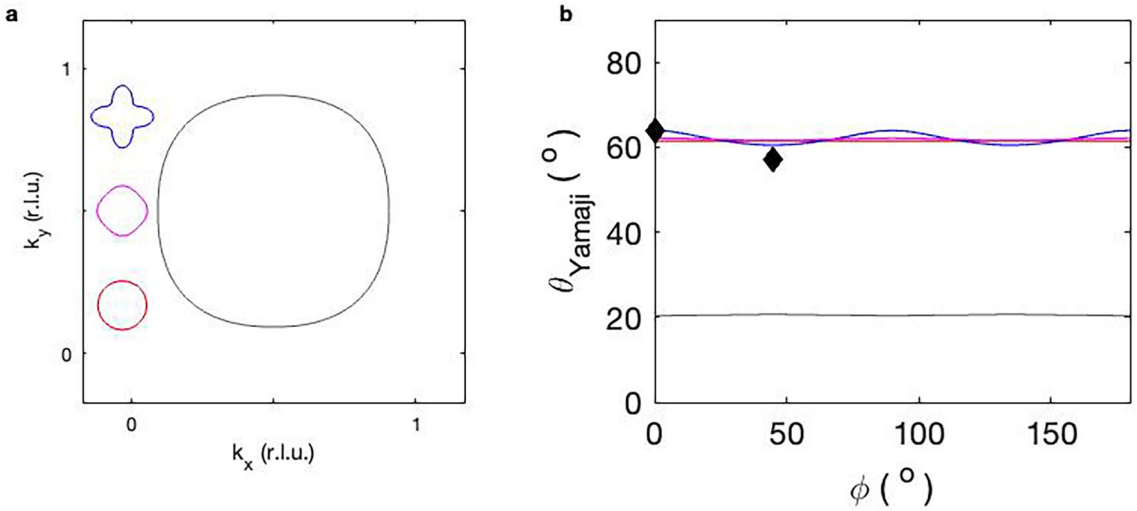

Extended Data Fig. 4 | Comparing Yamaji angle for Fermi surfaces with tetragonal planar symmetry. a, Planar cross-sections of model Fermi surfaces. The grey curve is the large Fermi surface expected for $1+p$ carriers in Hg1201[32,33]. The Fermi surface cross sections were generated with the function $k_{\|}(\phi_k) = [1 + \beta\cos(m\phi_k)]k_o$ following ref. 30. ϕ_k is the azimuthal angle of the Fermi momentum. $m = 4$ for planar tetragonal symmetry. β controls the deviation from a circular shape. For the small Fermi pockets $k_o = 0.15$ Å^{-1} and $\beta = 0$, 0.05 and 0.4 for the circle, diamond, and '+' shaped Fermi surfaces respectively. **b**, Calculated Yamaji angles θ_{Yamaji} as a function of ϕ[30], with simple sinusoidal warping. Colors are matched to the corresponding Fermi surfaces shown in panel **a**. θ_{Yamaji} was obtained for each ϕ by finding the zeros of the lowest order corrections to an un-warped Fermi surface cross-sectional area[30]: $A = J_0(\kappa) + A_2\cos(m\phi)$, where $A_2 = \beta(-1)^{m/2}[(1+m)J_m(\kappa) - \kappa J_{m+1}(\kappa)]$. $J_m(\kappa)$ are the Bessell functions of the m^{th} kind, $\kappa = ck_o\tan(\theta)$, c is the c-axis lattice parameter. Finally, m and k_o matches the values used to generate the specific Fermi surface cross-sections in **a**. The Yamaji condition for the leading term $J_0(\kappa) = 0$ yields the relationship for the Yamaji peak used in the main text, $\theta_{Yamaji} = \arctan[3\pi/(4ck_o)]$ with k_o replaced with k_{cal}. The second term, which accounts for a non-circular cross-section, yields a relatively small $\cos(m\phi)$ modulation about the first term. Therefore, our experimentally determined θ_{Yamaji} constrains the size of the pocket with tetragonal (or higher, since the same argument holds for $m = 6, 8, \ldots$) symmetry to the average Fermi momentum k_o. The large Fermi surface has $\theta_{Yamaji} \approx 20^\circ$, grey curve, that is clearly inconsistent with observations.

https://doi.org/10.1038/s41567-025-03032-2

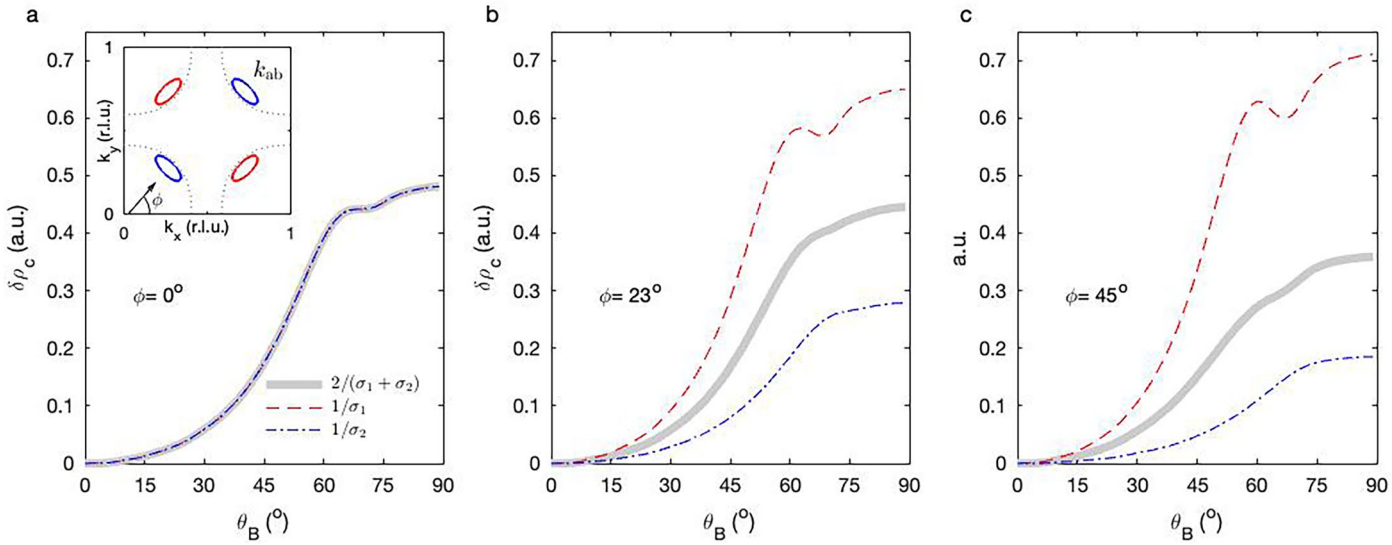

Extended Data Fig. 5 | Contribution of two sets of orthogonal ellipses to the resistivity. a, Simulated θ dependence of the magnetoresistivity $\delta\rho_c(\theta)$, with $\omega_c\tau = 2.6$, for each of the two orthogonally oriented ellipses (red and blue, see inset for schematic of the Fermi pockets color coded to match the curves) and the resultant combined contribution to $\delta\rho_c(\theta)$ of both sets of pockets (grey). The plotted combined $\delta\rho_c(\theta)$ curve includes an additional factor of two for easy comparison. For $\phi = 0^\circ$, $\delta\rho_c(\theta)$ is identical for the two sets of pockets. **b**, For $\phi = 23^\circ$, $\delta\rho_c(\theta)$ of each ellipse are no longer the same. While the Yamaji peak of the red curve is clearly discernible, the Yamaji effect manifests only as a broad kink in the blue curve. The θ_{Yamaji} of the two ellipse orientations are displaced such that the Yamaji peaks interfere destructively and is unobservable in the combined $\delta\rho_c(\theta)$ (grey). **c**, For $\phi = 4^\circ$ the Yamaji peak of the red curve is sufficiently displaced from the kink in the blue curve such that the Yamaji effect is discernible as a small bump in the combined $\delta\rho_c(\theta)$ (grey).

https://doi.org/10.1038/s41567-025-03032-2

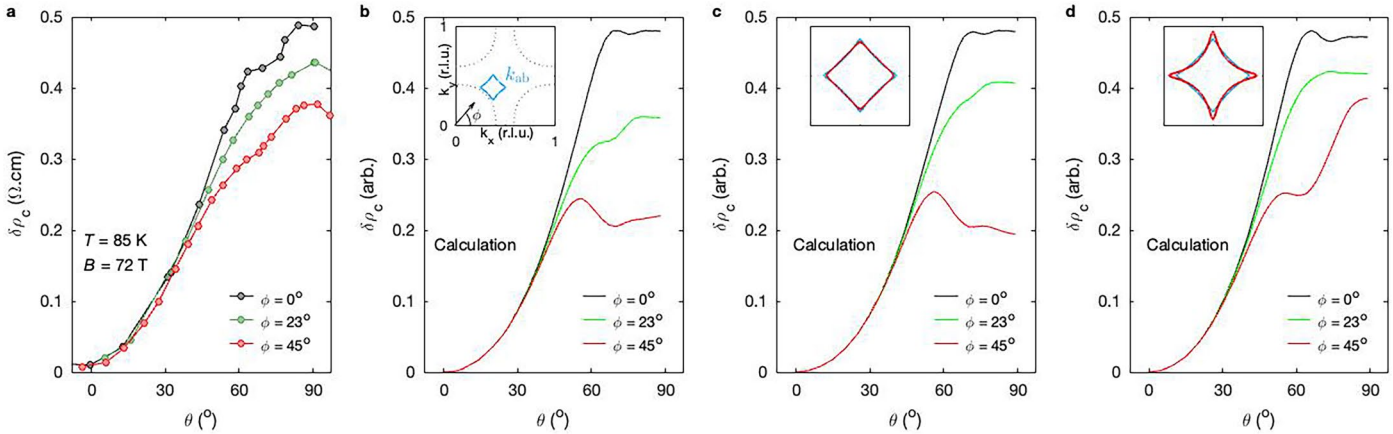

Extended Data Fig. 6 | Comparing measurements of angle dependent magnetoresistivity to expectations for a bi-axial charge-density-wave reconstruction. a, Magnetoresistivity $\delta\rho_c$ as a function θ for $\phi = 0^\circ$, 23° and 45°. **b**, Simulations for a reconstructed Fermi surface resulting from bi-axial charge-density-wave previously studied at low temperatures ($T \lesssim 4$ K)[12,39,40] This pocket has four-fold planar symmetry in agreement with the symmetry of the measured linear slope of magnetoresistivity $a_1(\phi)$ for in-plane fields, but it cannot capture the observed evolution of the Yamaji effect shown in panel **a**. **c** & **d**, Simulations for slight variations of the curvature of the reconstructed CDW pocket, while keeping the enclosed area of the pocket the same. The insets shows a closeup of the reconstructed pocket (reproduced from panel **b** inset) in blue and the modified pocket in red. Experimentally, the Yamaji peak for $\phi = 0^\circ$ is more pronounced than that for $\phi = 45^\circ$. The opposite is always found for simulations of the CDW pocket.

https://doi.org/10.1038/s41567-025-03032-2

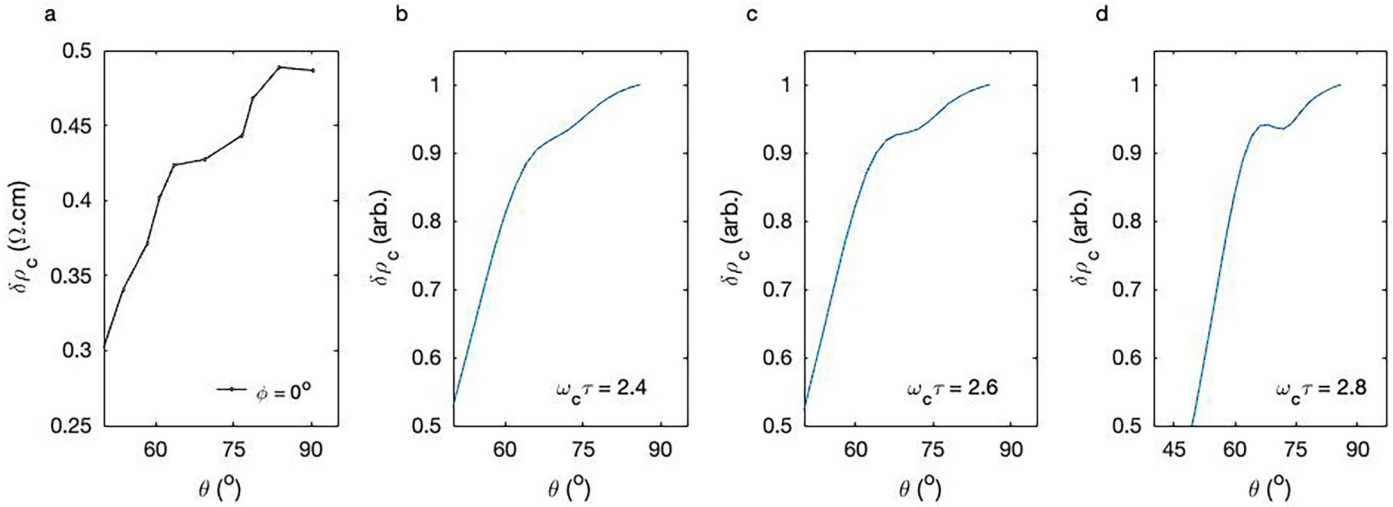

Extended Data Fig. 7 | Effect of changing $\omega_c\tau$ in modeling the Yamaji peak. a, Close up of the Yamaji peak in $\delta\rho_c(\theta)$ at $\phi = 0°$. It is compared to calculations from our model with varying $\omega_c\tau$ shown in panels **b**–**d**.